A Heat Flux Sensor based on Transpiration Cooling

Fabian Hufgard,[1] Stefan Loehle,[2] Hannah Boehrk,[3] Matthew McGilvray,[4] Johan Steelant,[5] Stefanos Fasoulas[6]

Abstract

In this paper the design of a novel heat flux sensor is presented. The sensor is based on the Pressure-Based Non-Integer System Identification (NISIp) method for a transpiration cooled material. Here, the pressure reading at the upstream side of the porous wall, the plenum, is used for the inverse determination of surface heat flux. For this, the pressure impulse response and measurement accuracy is found by laser calibration. Three sensors with equal design and geometry, but featuring different porous materials, zirconium diboride, carbon/carbon and copper, were investigated. The response time of a carbon/carbon sensor is significantly shorter than for the other materials. A maximum deviation of 8% to 13% was found for the presented NISIp sensors. The experimental investigation of different plenum volumes yields that the plenum volume has a damping effect on the temporal behaviour of the plenum pressure.

Keywords: *heat flux sensor, transpiration cooling, plenum pressure, NISIp, porous material*

Nomenclature

Latin

A − Area
a − Thermal diffusivity
C/C − Carbon/caron
c_p − Heat capacity
Cu − Copper
$D^{n/2}$ − (Non-integer) derivation operator
h_v − Volumetric heat transfer coefficient
K_D − Darcy permeability coefficient
K_F − Forchheimer permeability coefficient
L − Porous sample thickness
$\dot{m}$ − Mass flow rate
p − pressure
$\dot{q}$ − Surface heat flux

R − Specific gas constant for an ideal gas
T − Temperature
t − Time
V − Volume
x − Spatial variable
ZrB_2 − Zirconium diboride

Greek

α_n − NISI parameter
β_n − NISI parameter
λ − description Thermal conductivity
μ − Dynamic viscosity
ρ − Density
Φ − Porosity

[1]*PhD student, High Enthalpy Flow Diagnostics Group (HEFDiG), Institute of Space Systems, Pfaffenwaldring 29, 70569 Stuttgart, Germany, hufgard@irs.uni-stuttgart.de*

[2]*Research scientist, Group leader HEFDiG, Institute of Space Systems, Pfaffenwaldring 29, 70569 Stuttgart, Germany, loehle@irs.uni-stuttgart.de*

[3]*Research scientist, Group leader High Temperature Management for Hypersonic Flight, Institute of Structures and Design, DLR, Pfaffenwaldring 38-40, 70569 Stuttgart, Germany, hannah.boehrk@dlr.de*

[4]*Associate professor, Group leader Hypersonics group, Oxford Thermofluids Institute, The University of Oxford, Oxford OX2 0ES, United Kingdom, matthew.mcgilvray@eng.ox.ac.uk*

[5]*Senior research scientist, Flight Vehicles and Aerothermodynamics Engineering Section, ESA-ESTEC, Keplerlaan 1, P.O. Box 299, 2200 AG Noordwijk, Netherlands, johan.steelant@esa.int*

[6]*Professor, Director Institute of Space Systems, Pfaffenwaldring 29, 70569 Stuttgart, Germany, fasoulas@irs.uni-stuttgart.de*

Subscripts
$0 - x = 0$, i.e. at the surface
$c -$ Calibration
$f -$ Fluid

$m -$ Measurement
$pl -$ Plenum
$sim -$ Simulation

1. Introduction

Aerospace applications such as heat shields of re-entry vehicles or the internal wall structures of combustion chambers for rockets or (sc)ramjets are commonly subject to extreme thermal conditions, which prevent the usage of passively cooled structures and thus require active cooling [1–6]. Transpiration cooling is an active cooling technique, which promises to widen the range of hypersonic flight applications [7–10]. Transpiration cooling means that a fluid is passing through a porous wall and exiting into the ambient hot gas region. This has two favourable effects. Firstly, the fluid picks up some heat from the hot wall and carries it out of the system. The wall is thus actively cooled. Secondly, the fluid ejects into the boundary layer, which reduces the temperature in the boundary layer. Consequently, convective heat transfer into the wall is reduced. A detailed description of this process can be found e.g. in Böhrk et al. and in the references cited therein [7].

One essential parameter for the characterization of a transpiration cooling system is the net surface heat flux [11]. In this paper, a sensor system is presented, which allows for heat flux determination in transpiration cooled environments. Classical methods for surface heat flux determination as in [12, 13] fail in such a scenario, because of the coupled heat transfer between solid and fluid [14]. It was shown, however, that the pressure in the plenum, i.e. the enclosed volume behind the porous wall, is sensitive to the surface heat flux [15]. The presented sensor system uses this relation as a means for heat flux determination working with pressure as the actual measured quantity. Here, the transpiration cooled wall remains untouched, because the plenum pressure can be measured remotely. The sensor composition is described in section 3.

The underlying methodology of this sensor technology is the Pressure-Based Non-Integer System Identification approach (NISIp), which is being developed by the High Enthalpy Flow Diagnostics Group (HEFDiG) [15–21]. A review of this approach is given in section 2. Here, a given sensor system is calibrated using laser radiation. This yields the system's pressure impulse response, which fully characterizes the system and therefore provides its temporal behaviour [22]. The comparison of different impulse responses allows for conclusions about their underlying thermophysical systems.

Two different aspects of NISIp sensor behaviour are investigated in this work by analysis of the systems' impulse responses: The influence of the porous material itself and the effect of the magnitude of the plenum volume. For this reason, three NISIp sensors featuring different porous materials, zirconium diboride, copper and carbon/carbon, were characterized. This was done for three different plenum volumes.

2. Pressure-Based Non-Integer System Identification (NISIp)

2.1. Mathematical Background

The pressure in the plenum in a transpiration cooled system, i.e. the enclosed volume behind the porous wall, is sensitive to the surface heat flux [15]. The Pressure-Based Non-Integer System Identification (NISIp) approach enables the characterization of this relation for a given transpiration cooling system. This correlation of the plenum pressure $p_{pl}(t)$ to the net surface heat flux $\dot{q}_0(t)$ is given by [15, 16]

$$\sum_{n=M_0}^{M} \alpha_n D^{n/2} p_{pl}(t) = \sum_{n=L_0}^{L} \beta_n D^{n/2} \dot{q}_0(t) \qquad \text{with} \qquad \alpha_{M_0} = 1 \,. \qquad (1)$$

The equation was derived for different heat conduction problems using analytical approaches, where it originally was formulated with $T(t)$ instead of $p_{pl}(t)$ [23–25]. The adaptability from temperature to

pressure can be explained by the fact that the plenum pressure increase is caused by a temperature increase within the porous wall [15]. The porous wall temperature increases due to a surface heat flux. Conduction into the material and a temperature difference between coolant and porous wall leads to a heat transfer, i.e. a coolant temperature increase. The relation of fluid temperature $T(x,t)$ and pressure $p(x,t)$ within the porous wall is given by the Darcy-Forchheimer equation:

$$p\frac{\partial p}{\partial x}(x,t) = \frac{\mu_f(T(x,t))\,\dot{m}\,R\,T(x,t)}{K_D\,A} + \frac{\dot{m}^2\,R\,T(x,t)}{K_F\,A^2} \;, \quad (x,t) \geq 0 \tag{2}$$

with spatial and temporal variables x and t. The mass flow rate $\dot{m}$, the specific gas constant for an ideal gas R, the porous wall cross sectional area A and the material characteristic permeability coefficients K_D and K_F are assumed constant. The fluid's viscosity μ_f is a function of the fluid's temperature (Sutherland law). Hence, the local pressure $p(x,t)$ and pressure gradient $\frac{\partial p}{\partial x}(x,t)$ are a function of coolant temperature $T(x,t)$. A local increase of pressure and pressure gradient leads to an increased total pressure gradient over the wall and thus a higher plenum pressure [15].

2.2. Procedure of the NISIp Approach

The procedure of the NISIp approach is summarized in Fig. 1. During calibration, a well known heat flux is applied and the plenum pressure is measured using a commercial gauge. With the known heat flux and pressure profiles, the parameters α_n and β_n in Eq. 1 are found in the Identification step. This is done by simulating a pressure signal from the input heat flux and fitting it to the measured pressure profile using a least-squares approach.
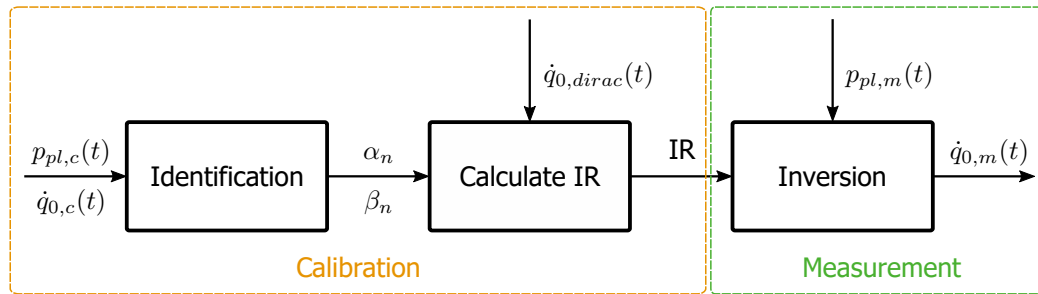

Fig. 1. Schematic of the procedure of the NISIp approach consisting of calibration and measurement; IR = impulse response, 0 = surface, pl = plenum, m = measurement, c = calibration.

In the second step of a NISIp calibration, the system's impulse response is calculated. A system's impulse response fully characterizes the system and therefore provides its temporal behaviour [22]. The comparison of different impulse responses allows for conclusions on their underlying thermophysical systems. A plenum pressure profile is calculated using Eq. 1 with the found set of parameters (α_n and β_n) and a numerical Dirac impulse as the input heat flux. The resulting pressure profile represents the system's impulse response. With this, the calibration stage is completed.

The measurement stage marks the last step of the NISIp procedure. Here, the found pressure impulse response is used for the determination of the net surface heat flux by deconvolution with the measured pressure profile using a Phased Van-Cittert inversion algorithm [26]. In this paper, a temporal heat flux profile is determined, which is provided by a diode laser and is thus well-known. This allows for an accuracy evaluation of the NISIp sensor and the found impulse responses by comparison of the measurement with the input heat flux.

3. NISIp Sensor

A schematic of the NISIp sensor is shown in Fig. 2. It consists of the porous sample, the pressure gauge, the mass flow controller and all parts enclosing the plenum, which includes the housing of the sensor

head (cf. Fig. 3) and tubing. In the calibration experiments the exact same NISIp sensor, including all of the involved sensor components, must be used as in the measurement scenario in order to ensure the applicability of the calibration to the measurement data. Nitrogen is fed from a reservoir at an absolute pressure of 9.5 bar into the mass flow controller.
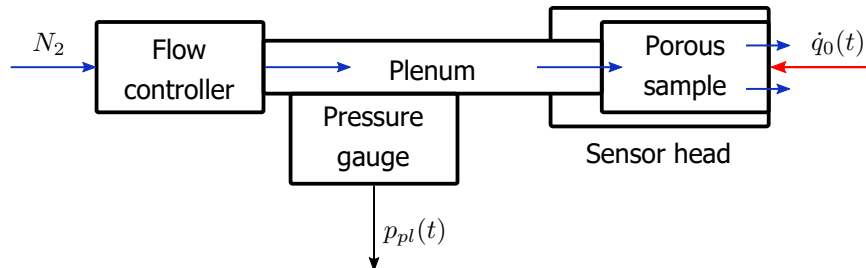

Fig. 2. Schematic of the NISIp sensor.

The sensor heads are depicted in Fig. 3. The porous samples' feature an equal geometry: a truncated cone with a draft angle of $10°$, a front diameter of 10.6 mm (smaller diameter of truncated cone) and a thickness L of 5 mm. The porous sample is pressed against the sensor housing by a set screw. Titanium *Ti6Al4V Grade 5* was chosen as the housing material due to its low thermal conductivity λ of $7.1\,W\,m^{-1}\,K^{-1}$. A low thermal conductivity is preferred in order to minimize lateral heat conduction into and out of the porous sample. A spring is inserted in between set screw and porous sample in order to account for thermal expansion. It transfers a force of 519 N onto a steel adapter plate, which evenly distributes the spring force onto the back face of the porous sample. A *Sigraflex* graphite foil acts as the sealant between porous sample and housing. A tube is integrated into the standard connector screw at the back of the sensor head. This tube connects the sensor head to the brass holder of the pressure gauge. The total length of the sensor head (including the connector screw) is 81 mm, the maximum diameter is 25 mm. The presented sensor head can be integrated into any structure onto which the heat flux shall be measured.
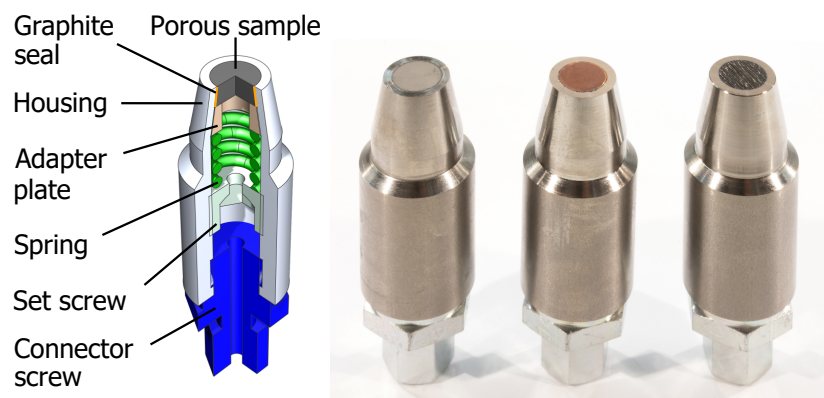

Fig. 3. NISIp sensor head with integrated porous samples; CAD and photo with ZrB_2, Cu and C/C from left to right.

Three different materials were used as the porous sample: zirconium diboride (ZrB_2), copper (Cu) and carbon/carbon (C/C). The ZrB_2 sample was manufactured and characterised at the Department of Materials of Imperial College London in collaboration with University of Oxford under the designation *UHTC-4 (pos)*. The designation *pos* means that the virgin porous material sample was abraded with sandpaper as described in [27]. The Cu sample was manufactured at the Fraunhofer Institute for Manufacturing Technology and Advanced Materials (IFAM) Dresden. The C/C sample was manufactured at the Institute of Structures and Design of German Aerospace Center (DLR) in Stuttgart. The material

characteristics of the porous materials are summarized in Table 1. The permeability coefficients of Cu were determined from the data shown in Fig. 5 and according to [27]. As can be seen in Fig. 3, the C/C sample was integrated such that the fibre layers are parallel to the flow direction. Therefore, the value for parallel heat conduction applies for a given thermal wave originating from the sample surface. The heat conduction normal to the fibre layers is $2\,\mathrm{W\,m^{-1}\,K^{-1}}$.

Table 1. Material characteristics of the investigated porous materials.

Material	λ $\mathrm{W\,m^{-1}\,K^{-1}}$	ρ $\mathrm{kg\,m^{-3}}$	c_p $\mathrm{J\,kg^{-1}\,K^{-1}}$	a $10^{-6}\,\mathrm{m^2\,s^{-1}}$	Φ %	K_D $10^{-15}\,\mathrm{m^2}$	K_F $10^{-9}\,\mathrm{m}$
ZrB$_2$	24.4 [28]	3538 [28]	437.6 [28]	15.8	41 [27]	9.12 [27]	7.48 [27]
Cu	200	4460	385	116	50	31.4	6.50
C/C	14 [7]	1400 [7]	1650 [7]	6.1	12.4 [29]	164.5 [7]	2900 [7]

As noted in Table 1, the permeability coefficients of C/C are significantly higher than for ZrB$_2$ and Cu, which means that C/C is the most permeable material among the three. Cu features a higher K_D value than ZrB$_2$, whereas their K_F values are almost equal. ZrB$_2$ is therefore the least permeable material among the three analysed materials. This order also reflects in Fig. 5, because ZrB$_2$ shows the steepest rise of plenum pressure over mass flow rate and C/C the most gradual.

The thermal diffusivity of each material is shown in Table 1. The thermal diffusivity a of Cu is two orders of magnitude higher than that of ZrB$_2$ and C/C. This means that the Cu sample distributes a given surface heat pulse significantly quicker into the material, which leads to a fast equalization of the spatial temperature field within the porous sample. C/C features a slightly lower thermal diffusivity than ZrB$_2$.

The mass flow controller used is a *Tylan FC 2901 4S* with an accuracy of 1% and a response time of 500 ms. It provides a constant mass flow rate during the course of a given calibration measurement and was operated with an in-house controller. The mass flow is additionally measured by a mass flow meter *Siemens Sitrans F C Massflo Mass 2100* with an accuracy of 0.1% of the measurement, which was located upstream the mass flow controller. The setting accuracy is $\pm\,0.5\,\mathrm{mg\,s^{-1}}$. It is fed by a Nitrogen reservoir at a total pressure of 9.5 bar. The pressure gauge is a *Yokogawa EJA530E* with an accuracy of 27.5 mbar and a response time of 90 ms. The gas temperature in the plenum is measured using a Pt100 resistance thermometer. It is located in the brass holder of the pressure gauge. The plenum gas temperature remained constant within 0.31 K over the course of a given measurement.

The tube at the back side of the sensor head is connected to the brass holder of the pressure gauge. The size of this tube was varied in different experiments in order to investigate the effect of the size of the plenum volume on the behaviour of the plenum pressure. The total plenum volume spans from the outlet of the mass flow controller to the backside of the porous sample. The smallest plenum volume of $V_{pl,1} = 23.3 \pm 1.4\,\mathrm{cm^3}$ was made up by a 616 mm long tube with an inner diameter of 4 mm. The two other plenum volumes were realized by placing an additional tube with a diameter of 10 mm between the pressure gauge brass holder and the 4 mm tube. With the additional tube length of 120 and 268 mm and accounting for associated connecting parts, the plenum volumes amount to $V_{pl,2} = 35.0 \pm 2.4\,\mathrm{cm^3}$ and $V_{pl,3} = 46.7 \pm 3.3\,\mathrm{cm^3}$. This corresponds to $V_{pl,2} = 1.5\,V_{pl,1}$ and $V_{pl,3} = 2\,V_{pl,1}$.

4. Sensor Calibration

The different NISIp sensor systems are assessed by comparison of their respective impulse responses. A sensors' impulse response is found in the calibration stage of the NISIp approach (cf. Fig. 1). The experimental setup for calibration and the procedure of a NISIp sensor calibration are described in this section. Additionally, a known temporal heat flux profile is applied to the surface and at the same time it is determined by means of the NISIp method using the acquired impulse responses. The deviation of the determined heat flux from the input heat flux quantifies the sensor accuracy.

4.1. Experimental Setup for Calibration

The NISIp sensor calibration is conducted using the laser calibration test stand at the Institute of Space Systems, Stuttgart. The experimental setup is shown in Fig. 4. The sensor head is located in the centre of a 50 mm diameter copper half sphere. The half sphere as well as its brass mount are water cooled. A narrow air gap insulates the sensor head from the copper half sphere. The pressure gauge and the mass flow controller are located peripherally.
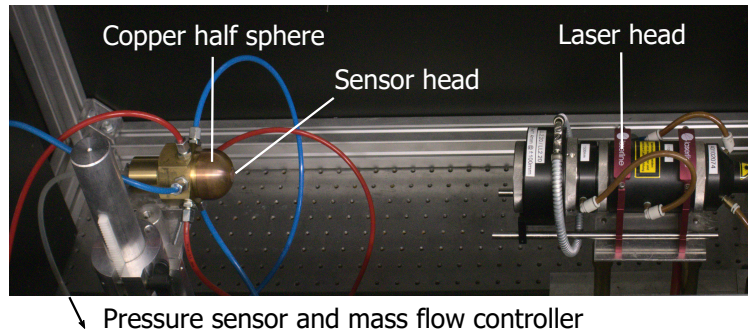

Fig. 4. Experimental setup for calibration.

Radiative heating is provided by an infrared diode laser (*Laserline LDM 500-100*) with a peak power of 540 W a wavelength of 910 nm and a power rise time of < 0.1 ms. The laser head evenly distributes the beam into a squared profile of 34.1 x 34.1 mm^2 at the distance of 300 mm. The beam overlaps the porous sample in order to mitigate lateral heat conduction. The laser demand can be recalculated to the optical laser power using the manufacturer's specifications. From this, the beam area and the absorptivity of the porous samples, the heat flux can be calculated. The plenum pressure and the laser demand were acquired using an oscilloscope *LeCroy WaveSurver 24 Xs-A*.

4.2. Calibration Procedure

Figure 5 gives an overview over the investigated initial conditions for which the NISIp sensors were characterized. All NISIp sensors were characterized at the same mass flow rate of 60 mg s^{-1} in order to compare their impulse response behaviour at comparable conditions. For the same reason, an experiment with an initial pressure difference to the ambient pressure of 4 bar was conducted for each material. In order to set the mass flow rate of 60 mg s^{-1} into context for a given porous material, the systems were each characterized at three other mass flow rates. The experimental hardware limits the mass flow rate to 30 - 200 mg s^{-1} and a maximum initial plenum pressure of 6 bar. Four evenly distributed mass flow rates were chosen for each material, where one mass flow rate was 60 mg s^{-1} for each material (cf. Fig. 5).

At the start of a calibration experiment, a steady state flow condition is setup before the calibration heat flux is applied to the surface. During radiative heating, the plenum pressure is recorded, which gives data sets as shown exemplarily in Fig. 6a. In this figure, the initial plenum pressure difference to ambient is 4 bar for each material. The plenum pressure traces differ between the tested materials. One obvious reason is a difference in net surface heat flux, which affects the porous samples. This difference can be seen in Fig. 6a and is due to a difference in absorptivity. The absorptivity of the porous materials at the laser wavelength are: 0.75 (ZrB$_2$) [30,31], 0.6 (Cu) [32] and 0.88 (C/C) [7]. The incident radiative heat flux was equal between tests: An optical power of 540 W is evenly distributed over the squared beam profile. Aside from the absorptivity, the system's plenum pressure impulse response is the main driver of the plenum pressure history.

From a given data set such as shown in Fig. 6a, the impulse response can be calculated. For this, the NISI parameters α_n and β_n (Eq. 1) are identified for the given heat flux and plenum pressure curves.
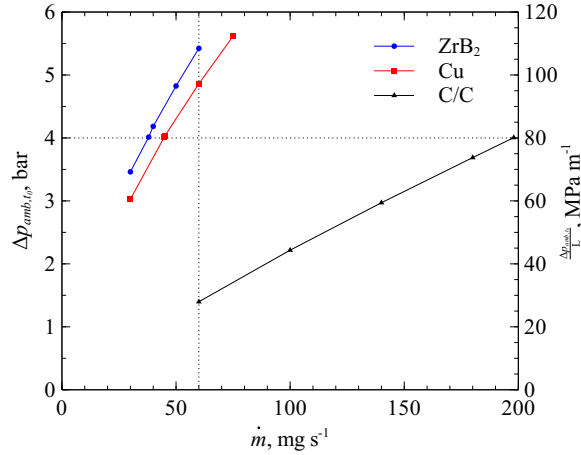
Fig. 5. Overview over the initial conditions for each analysed flow case; Initial pressure difference to ambient $\Delta p_{amb,t_0}$ over mass flow rate $\dot{m}$; dotted horizontal and vertical lines indicate data sets for the comparison between different porous materials ($\dot{m} = 60\,\mathrm{mg\,s^{-1}}$ and $\Delta p_{amb,t_0} = 4\,\mathrm{bar}$).

For all data sets in this work, Eq. 1 was used with four sum terms on the pressure side and five on the heat flux side:

$$
\begin{aligned}
(\alpha_1 D^{-0.5} + \alpha_2 + \alpha_3 D^{0.5} + \alpha_4 D)p_{pl}(t) \\
= (\beta_1 D^{-1} + \beta_2 D^{-0.5} + \beta_3 + \beta_4 D^{0.5} + \beta_5 D)\dot{q}_0(t)\,.
\end{aligned}
\tag{3}
$$

Using Eq. 3 the measured pressure data were reproduced for the incident calibration heat flux. Using a least squares approach, the resulting simulated pressure is fitted to the measured pressure. The best fit for the data in Fig. 6a is shown in Fig. 6b. The simulated and measured pressure curves match nicely. This procedure results in a separate parameter set (α_n and β_m) for each data set. The found parameters are used together with a numerical Dirac impulse to calculate the plenum pressure impulse response. The numerical Dirac impulse is a heat flux of $6.02\,\mathrm{W\,m^{-2}}$ for one time step. With the time step length of $166\,\mathrm{ms}$ this corresponds to a heat density of $1\,\mathrm{J\,m^{-2}}$. The resulting impulse responses are presented and discussed in the following.

5. Results

Three aspects of the plenum pressure impulse responses are analysed in this section. The influence of the porous material itself on the qualitative impulse response shape is discussed in subsection 5.1. The mass flow rate dependant behaviour for all three materials is analysed in subsection 5.2. Subsection 5.3 addresses the effect of the plenum volume size.

5.1. Comparison between Porous Materials

The impulse responses for a mass flow rate of $60\,\mathrm{mg\,s^{-1}}$ and for an initial plenum pressure difference to ambient of 4 bar are shown in Fig. 7. The impulse responses of ZrB_2 and Cu are qualitatively comparable. C/C shows a more distinct response, i.e. the initial rise to the peak and the subsequent drop are significantly steeper for C/C. This impulse response shape is assessed as beneficial for the determination of surface heat flux. The magnitude of plenum pressure peak is higher for ZrB_2 than for Cu in both comparison cases shown in Fig. 7. For a mass flow rate of $60\,\mathrm{mg\,s^{-1}}$, the magnitude of the C/C impulse response is lower than the other two (cf. Fig. 7a). For an initial pressure difference to ambient of 4 bar, the peak pressure of C/C is higher than for ZrB_2 and Cu.

The impulse response behaviour is connected to the soild and fluid temperature within the porous wall, because the plenum pressure increase is caused by the fluid temperature increase within the porous wall, as described in subsection 2.1. The thermal diffusivity is one main driver in the evolution of the porous
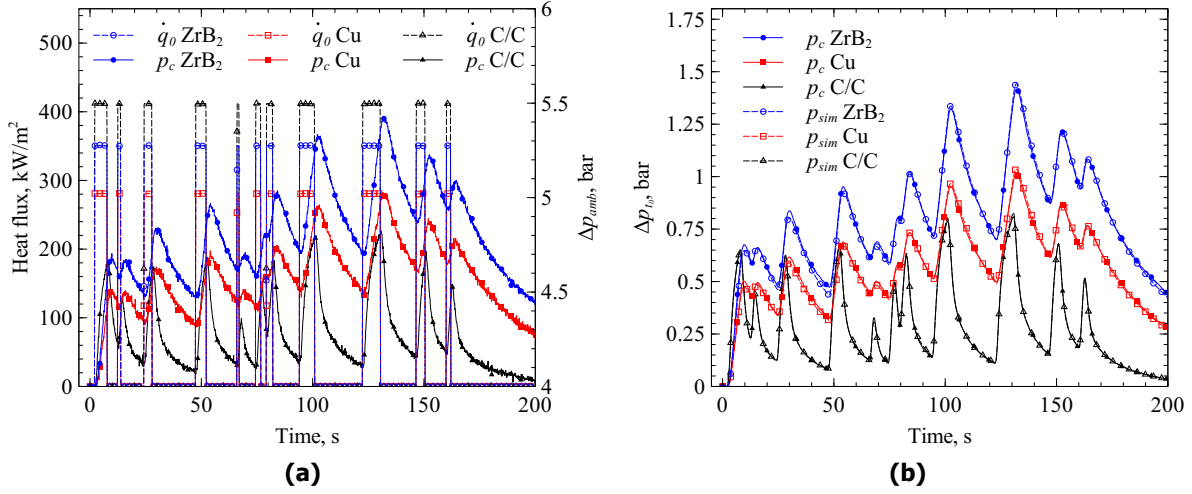
Fig. 6. (a): Calibration datasets for all materials at 4 bar initial pressure difference to ambient (Δp_{amb}); (b): best fits of simulated plenum pressure difference p_{sim} to the measured plenum pressure difference p_c with the pressure difference to initial pressure Δp_{t_0}.

wall temperature field. C/C features a relatively low thermal diffusivity of $6.1 \cdot 10^{-6}\,\mathrm{m^2\,s^{-1}}$ compared to ZrB$_2$ and Cu ($15.8 \cdot 10^{-6}\,\mathrm{m^2\,s^{-1}}$ and $116 \cdot 10^{-6}\,\mathrm{m^2\,s^{-1}}$). The thermal wave reaches not as far into the C/C sample before it is damped through convective cooling and the heat is carried out of the system by the coolant. The C/C impulse response depicted in Fig. 7a might therefore be lower in magnitude and reaching its peak quicker than the ZrB$_2$ and Cu impulse responses.

Another significant parameter in the transient transpiration cooling process is the volumetric heat transfer coefficient h_v. The h_v values of the transpiration cooling conditions of the impulse responses shown in Fig. 7 are given in Table 2. These values are determined by the Nusselt correlation [7, 33]

$$h_{v,Nu} = Nu\,\frac{\lambda_f}{K_D} = 2.22 \cdot 10^{-6}\,\frac{\lambda_f}{K_D}\left(\frac{\dot{m}\,\sqrt{K_D}}{\mu_f\,A_{mean}}\right)^{0.703} \tag{4}$$

with the fluid thermal conductivity λ_f and dynamic viscosity μ_f and the sample's mean cross-sectional area $A_{mean} = (\varnothing_{mean}/2)^2 \cdot \pi$ with $\varnothing_{mean} = \varnothing_{front} + tan(10°) \cdot L = 11.5\,\mathrm{mm}$ and the front diameter $\varnothing_{front} = 10.6\,\mathrm{mm}$. h_v scales the transfer of thermal energy between solid and fluid and thus the relation between surface heat flux and plenum pressure, because the heat flux affects the solid temperature and the plenum pressure is a function of fluid temperature. Considering this, a high h_v should boost both the magnitude of the impulse response peak and the time until the peak is reached. However, the h_v of C/C is lower than that of ZrB$_2$ as can be seen from Table 2 and the C/C impulse response reaches its peak quicker. This suggests, that h_v plays a minor role for the plenum pressure impulse response.

Table 2. Volumetric heat transfer coefficients calculated from Eq. 4 [7, 33] for the underlying conditions of the impulse responses shown in Fig. 7.

Material	$h_v(60\,\mathrm{mg\,s^{-1}})$, $\mathrm{W\,m^{-3}\,K^{-1}}$	$h_v(4\,\mathrm{bar})$, $\mathrm{W\,m^{-3}\,K^{-1}}$
ZrB$_2$	$1.11 \cdot 10^5$	$8.03 \cdot 10^4$
Cu	$2.34 \cdot 10^4$	$1.91 \cdot 10^4$
C/C	$1.70 \cdot 10^4$	$3.92 \cdot 10^4$

The performance of the NISIp sensors and their respective impulse responses shown in Fig. 7a were determined by the analysis of a well-known heat flux profile, which is temporally shaped like a Gauss
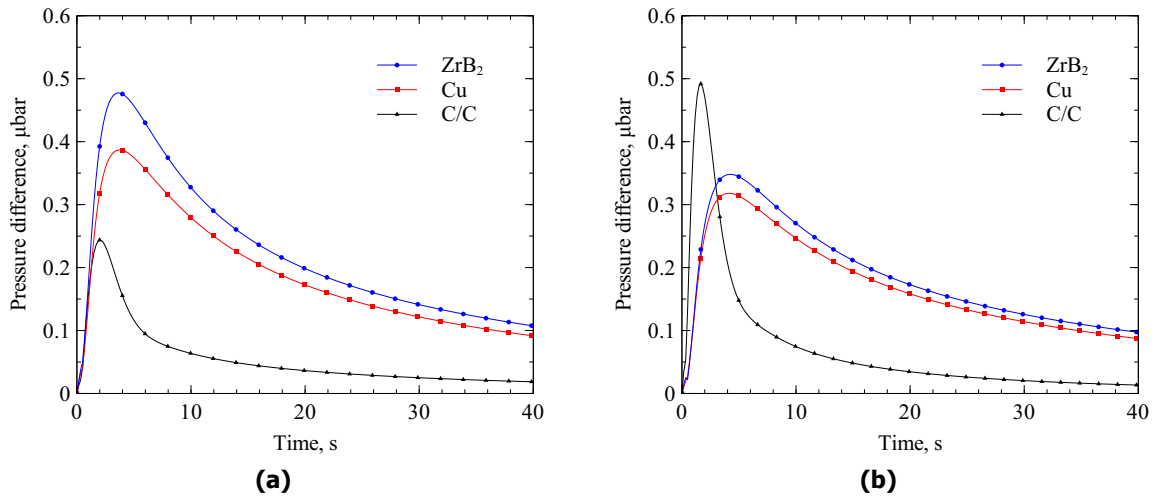
Fig. 7. Plenum pressure impulse responses to a Dirac heat flux impulse of $1\,J\,m^{-2}$ for all porous materials at $60\,mg\,s^{-1}$ (a) and an initial pressure difference to ambient of $4\,bar$ (b).

profile. The determined heat flux profiles are shown with the input heat flux and the plenum pressure signal in Fig. 8a. As can be seen, the determined heat flux matches the input nicely. The deviation (relative to the peak input value) of the determined heat flux is shown in Fig. 8b. It is $< 13.1\%$ for ZrB_2, $< 12.6\%$ for Cu and $< 7.61\%$ for C/C.
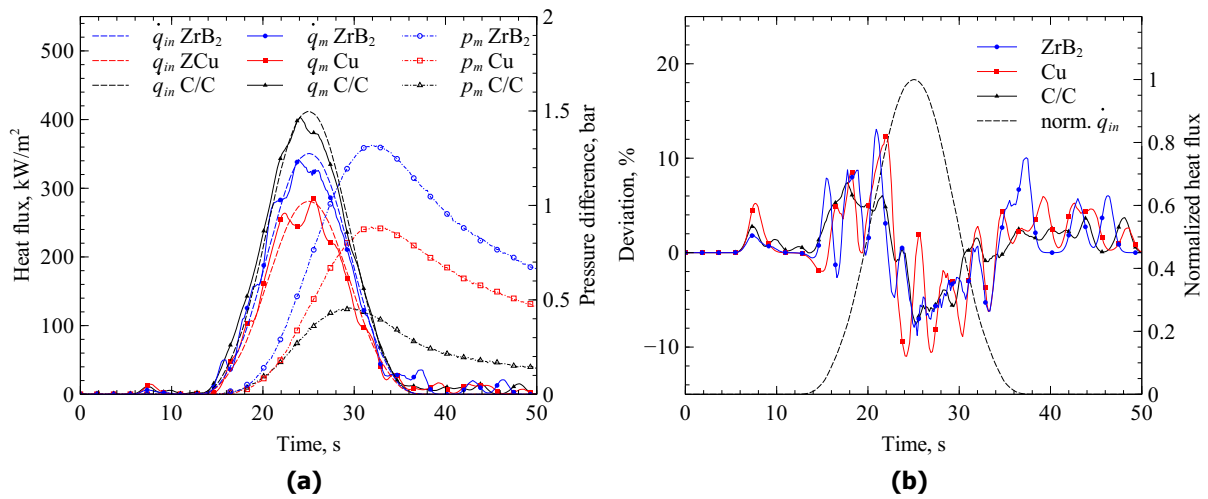

Fig. 8. Measured pressure profiles p_m due to Gauss shaped input heat flux $\dot{q}_{in}$ and determined surface heat flux $\dot{q}_m$ (a) and deviation of $\dot{q}_m$ from $\dot{q}_{in}$ relative to peak input heat flux (b).

5.2. Mass Flow Rate Dependency

The dependency of the plenum pressure impulse responses on the mass flow rate has been addressed in earlier studies already [16–18]. However, in this work the first direct comparison is drawn between different materials and for equal transpiration cooling systems, i.e. porous sample geometry and plenum volume ($23.3 \pm 0.7\,cm^3$). In separate experiments, the mass flow rate was varied. Figures 9a, 9b and 9c show the impulse responses of these experiments for ZrB_2, Cu and C/C. It can be seen that the shape

of the plenum pressure impulse response depends on the coolant mass flow rate. The impulse response peak pressure increases with mass flow rate. This holds true for each material.
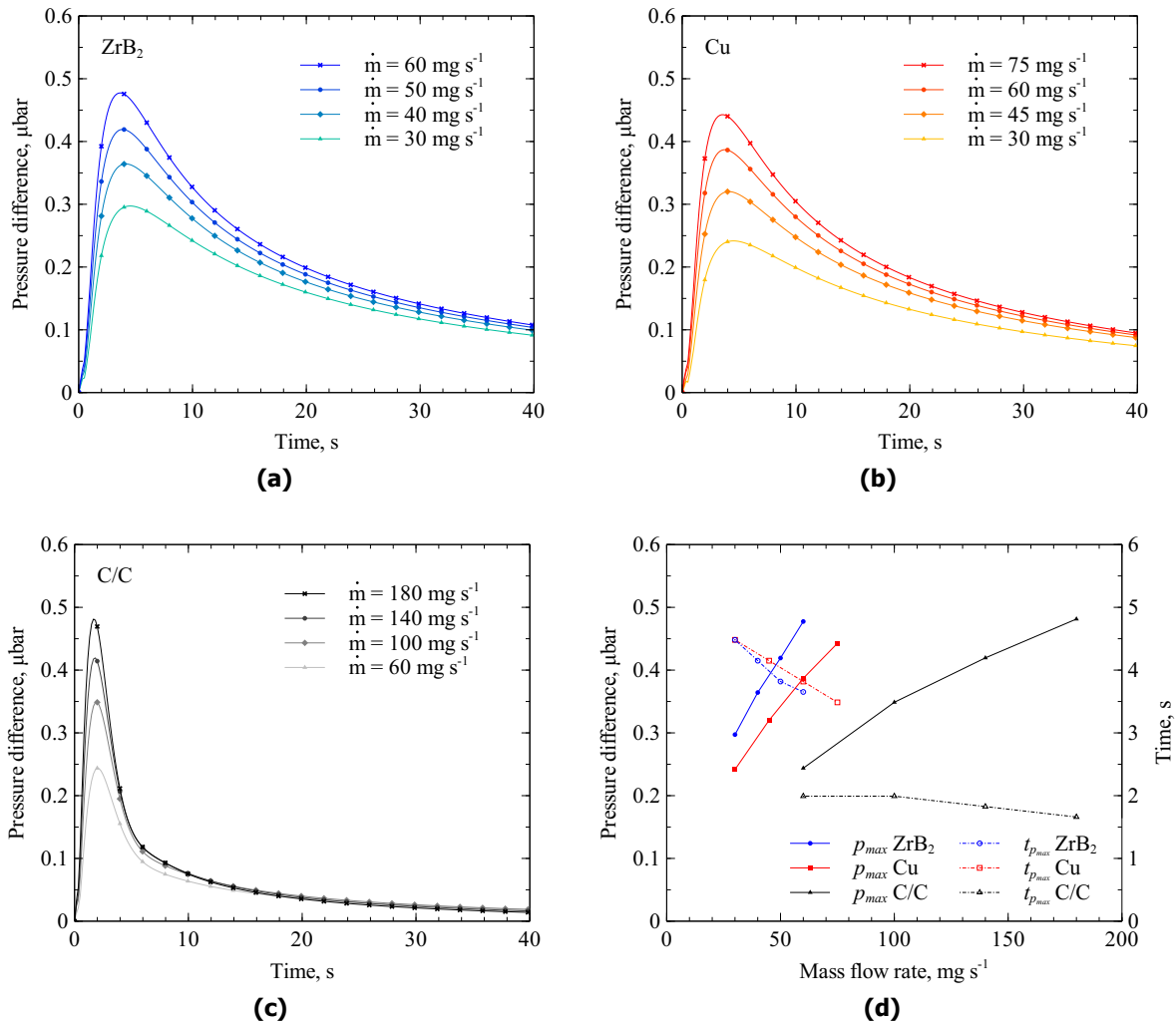

Fig. 9. Plenum pressure impulse responses to a Dirac heat flux impulse of $1\,\mathrm{J\,m^{-2}}$ for various mass flow rates and each porous material, C/C (a), Cu (b) and ZrB$_2$ (c); impulse response peak behaviour over mass flow rate (d).

The ratio at which the peak pressure increases with the mass flow rate is visualized in Fig. 9d. ZrB$_2$ shows the steepest peak increase over mass flow rate, C/C the weakest. One reason is that ZrB$_2$ is the least permeable material among the tested ones.

The time until the impulse responses reach their respective peak pressure is shown in Fig. 9d. All C/C impulse responses reach their peak significantly earlier than the ZrB$_2$ and Cu impulse responses. This shows that the findings from subsection 5.1, where the impulse responses were compared for a mass flow rate of $60\,\mathrm{mg\,s^{-1}}$, are valid for all tested mass flow rates. The time until the peak is reached decreases with increasing mass flow rate. This decrease is slightly steeper for ZrB$_2$ than for Cu. C/C shows a weak decrease.

5.3. Damping Effect of Plenum Volume

It was shown theoretically, that the plenum volume has a damping effect on the plenum pressure impulse response [18]. This theory is demonstrated experimentally by the impulse responses for different plenum volume sizes, which are shown in Figs. 10a, 10b and 10c. The original plenum volume of $23.3 \pm 1.4\,cm^3$ was increased to its 1.5-fold and its 2-fold size. The mass flow rate was $60\,mg\,s^{-1}$ in each case. It can be seen in Figs. 10a to 10c, that the impulse response peak is lower in magnitude and is reached later for increasing plenum volume size. That means that the impulse response is damped by an increasing plenum volume size. A clearer visualisation of this behaviour is shown in Fig. 10d. The rate of peak pressure decrease over plenum volume is similar for all three materials. The peak pressure decreases by 11% (C/C) to 16% (ZrB_2) when doubling the plenum volume. The time until peak increases stronger for ZrB_2 and Cu than for C/C: 55 and 49% for ZrB_2 and Cu, 25% for C/C.
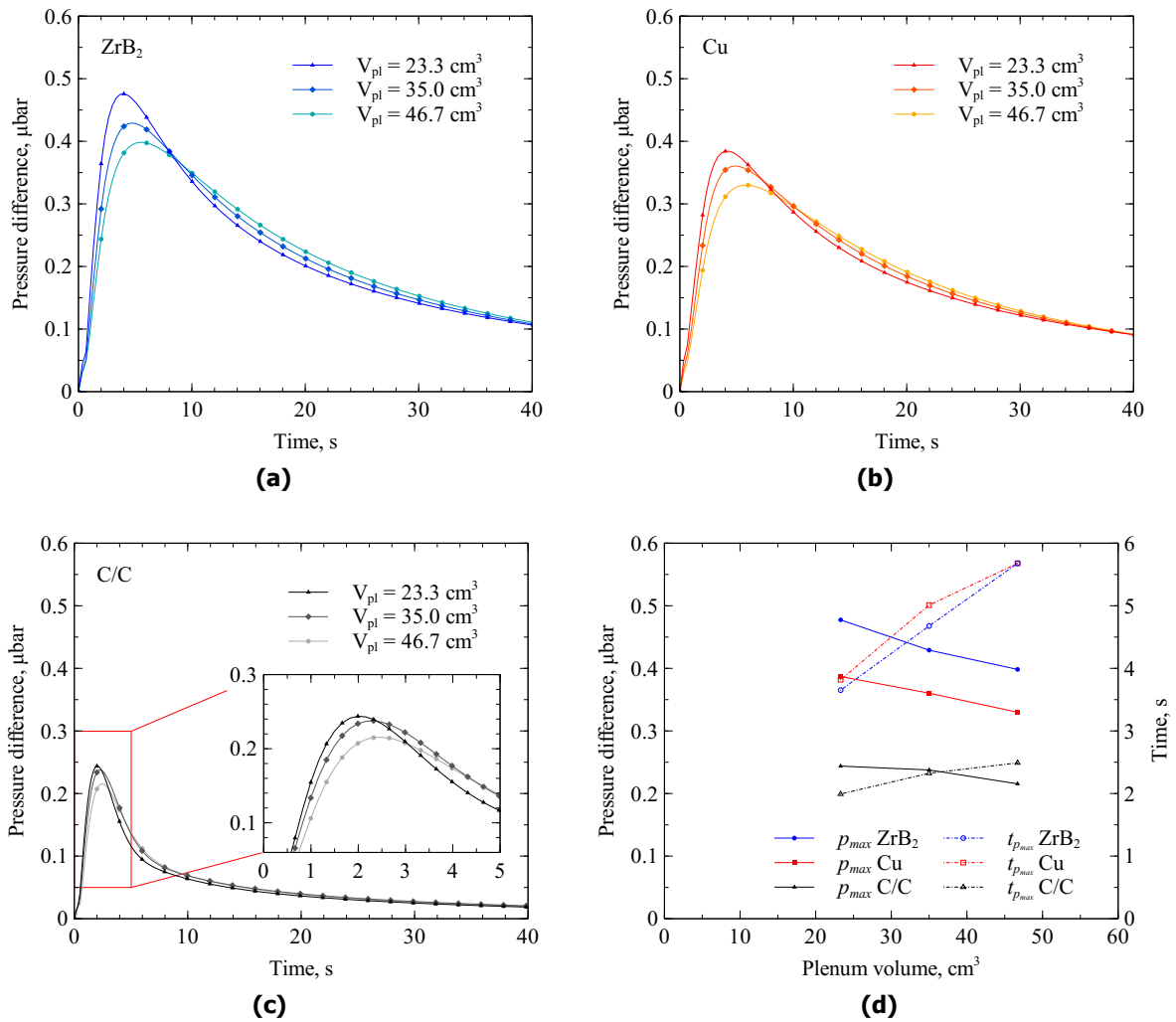

Fig. 10. Plenum pressure impulse responses to a Dirac heat flux impulse of $1\,J\,m^{-2}$ for various plenum volumes at $60\,mg\,s^{-1}$ and each porous material C/C (a), Cu (b) and ZrB_2 (c); impulse response peak behaviour over plenum volume size (d).

6. Summary and Conclusion

This paper presents investigations performed with a transpiration cooled heat flux sensor featuring different porous samples with equal geometry. The sensor composition and calibration and the experimental setup are described in detail. Plenum pressure impulse responses were calculated for various transpiration cooling conditions. The impulse responses of the different porous materials were compared for equal transpiration cooling conditions. The C/C sensor features a more distinct impulse response, which renders it more suitable for heat flux determination. This is confirmed by an accuracy evaluation, where a known surface heat flux was determined. An accuracy of $< 13.1\%$ is reached for ZrB_2, $< 12.6\%$ for Cu and $< 7.61\%$ for C/C.

Additionally, impulse responses are presented for different mass flow rates. The dependency of the impulse responses on mass flow rate is similar between ZrB_2 and Cu. C/C is less sensitive in this respect. These results show, that the findings of the impulse response comparison at a mass flow rate of $60\,\mathrm{mg\,s^{-1}}$ hold true for all tested mass flow rates.

The plenum pressure size was varied in different tests. The results prove that the plenum pressure impulse responses are damped by an increasing plenum volume. This dependency is similar for all materials.

In conclusion, the optimal sensor design consists in a small plenum volume and a highly permeable porous material. Higher cooling mass flow rates increase the sensor's sensitivity, too. Out of the tested materials, C/C was identified as the most suitable for the inverse determination of surface heat flux from plenum pressure.

7. Acknowledgements

References

[1] W. M. Kays. Heat transfer to the transpired turbulent boundary layer. *International Journal of Heat and Mass Transfer*, 15(5):1023–1044, 1972.

[2] Ernst Arne Meese and Helge Nørstrud. Simulation of convective heat flux and heat penetration for a spacecraft at re-entry. *Aerospace Science and Technology*, 6(3):185–194, 2002.

[3] John J. Bertin. *Hypersonic aerothermodynamics*. AIAA education series. American Institute of Aeronautics and Astronautics, Washington, DC, 1994.

[4] James M. Mulcahy, David J. Browne, Kenneth T. Stanton, Franklin R. Chang Diaz, Leonard D. Cassady, Daniel F. Berisford, and Roger D. Bengtson. Heat flux estimation of a plasma rocket helicon source by solution of the inverse heat conduction problem. *International Journal of Heat and Mass Transfer*, 52(9-10):2343–2357, 2009.

[5] J.A Nesbitt. Thermal modeling of various thermal barrier coatings in a high heat flux rocket engine. *Surface and Coatings Technology*, 130(2-3):141–151, 2000.

[6] L. Strand, M. Jones, R. Ray, and N. Cohen. Characterization of hybrid rocket internal heat flux and htpb fuel pyrolysis. In *30th Joint Propulsion Conference and Exhibit*, Reston, Virigina, 1994. American Institute of Aeronautics and Astronautics.

[7] H. Boehrk, O. Piol, and M. Kuhn. Heat balance of a transpiration-cooled heat shield. *Journal of Thermophysics and Heat Transfer*, 24(3):581–588, 2010.

[8] H. Boehrk. Transpiration-cooled hypersonic flight experiment: Setup, flight measurement, and reconstruction. *Journal of Spacecraft and Rockets*, 52(3):674–683, 2015.

[9] T. Langener, J. von Wolfersdorf, and J. Steelant. Experimental investigations on transpiration cooling for scramjet applications using different coolants. *AIAA Journal*, 49(7):1409–1419, 2011.

[10] K. D. Basore, M. Selzer, V. Wheatley, R. R. Boyce, D. J. Mee, B. R. Capra, M. Kuhn, and S. Brieschenk. Performance comparison of distributed injection methods for hypersonic film-cooling. In *Proceedings of the 20th Ausrtralasian Fluid Mechanics Conference*, 2016.

[11] T. Hermann, M. McGilvray, and I. Naved. Performance of transpiration-cooled heat shields for reentry vehicles. *AIAA Journal*, 58(2):830–841, 2020.

[12] M. N. Ozisik. *Heat Conduction*. Wiley, 2nd edition edition, 1993.

[13] J. Beck, B. Blackwell, and C. R. St. Clair. *Inverse Heat Conduction: Ill-posed Problems*. Wiley, 1985.

[14] O. M. Alifanov. *Inverse Heat Transfer Problems*. Springer Science & Business Media, Berlin Heidelberg, 2012.

[15] S. Loehle, S. Schweikert, and J. von Wolfersdorf. Method for heat flux determination of a transpiration cooled wall from pressure data. *Journal of Thermophysics and Heat Transfer*, 30(3):567–572, 2016.

[16] F. Hufgard, S. Loehle, T. Hermann, S. Schweikert, M. McGilvray, J. von Wolfersdorf, J. Steelant, and S. Fasoulas. Analysis of porous materials for transpiration cooled heat flux sensor development. In *HiSST*, Moscow, Russia, 2018.

[17] F. Hufgard, S. Loehle, J. von Wolfersdorf, S. Fasoulas, M. Ewenz Rocher, T. Hermann, M. McGilvray, and J. Steelant. Surface heat flux measurement in transpiration cooled porous materials using plenum pressure data. In *SciTech 2019*, Reston, VA, USA, 2019. AIAA.

[18] F. Hufgard, S. Loehle, M. McGilvray, T. Hermann, S. Schweikert, J. von Wolfersdorf, J. Steelant, and S. Fasoulas. Plenum pressure behavior in transiently heat loaded transpiration cooling system. *Journal of Thermophysics and Heat Transfer*, 35(2):256–267, 2021.

[19] F. Hufgard, S. Loehle, and S. Fasoulas. Heat flux determination from pressure data in transpiration cooling experiment. In *ICIPE*. 2022.

[20] F. Hufgard, C. Duernhofer, S. Fasoulas, and S. Loehle. A transpiration cooled heat flux sensor utilizing plenum pressure: Measurement in high enthalpy flow. In *FAR - 2nd International Conference on Flight Vehicles, Aerothermodynamics and Re-entry Missions & Engineering*, Noordwijk, The Netherlands, 2022. ESA Publications Division.

[21] F. Hufgard, C. Duernhofer, S. Loehle, S. Schweikert, C. Mueller, G. Di Martino, H. Boehrk, J. Steelant, and S. Fasoulas. Adjusting transpiration cooling to real time surface heat flux estimation. In *HiSST*, Brugge, BE, 2022.

[22] L. Ljung. *System Identification: Theory for the User*. Prentice Hall, Upper Saddle River, NJ, USA, 1987.

[23] J.-L. Battaglia, O. Cois, L. Puigsegur, and A. Oustaloup. Solving an inverse heat conduction problem using a non-integer identified model. *International Journal of Heat and Mass Transfer*, 44:2671–2680, 2001.

[24] J.-L. Gardarein, J.-L. Battaglia, and S. Loehle. Heat flux sensor calibration using noninteger system identification: Theory, experiment, and error analysis. *Review of Scientific Instruments*, 80(025103), 2009.

[25] S. Loehle. Derivation of the non-integer system identification method for the adiabatic boundary condition using laplace transform. *International Journal of Heat and Mass Transfer*, 115:1144–1149, 2017.

[26] P. H. van Cittert. Zum einfluss der spaltbreite auf die intensitätsverteilung in spektrallinien. *Zeitschrift für Physik*, 65(547), 1931.

[27] H. S. Ifti, T. Hermann, and M. McGilvray. Flow characterisation of transpiring porous media for hypersonic vehicles. In *22nd AIAA International Space Planes and Hypersonics Systems and Technologies Conference*, Reston, VA, USA, 2018. AIAA.

[28] T. Hermann, H. S. Ifti, M. McGilvray, L. Doherty, and R. P. Geraets. Mixing characteristics in a hypersonic flow around a transpiration cooled flat plate model. In *HiSST*, Moscow, Russia, 2018.

[29] M. Selzer, S. Schweikert, H. Boehrk, H. Hald, and J. von Wolfersdorf. Comprehensive c/c sample characterizations for transpiration cooling applications.

[30] M. Ewenz Rocher, T. Hermann, M. McGilvray, H. S. Ifti, F. Hufgard, M. Eberhart, A. Meindl, S. Loehle, and F. Zander. Testing a transpiration cooled zirconium-di-boride sample in the plasma tunnel at irs. In *SciTech 2019*, Reston, VA, USA, 2019. AIAA.

[31] M. Balat-Pichelin, E. Bêche, D. Sciti, and D. Alfano. Emissivity, catalycity and microstructural characterization of zrb2sicfiber based uhtc at high temperature in a non-equilibrium air plasma flow. *Ceramics International*, 40(7 Part A):9731–9742, 2014.

[32] Y. S. Touloukian, D. P. Dewitt, and R. S. Hernicz. *Thermal radiative properties: Coatings*. 1972.

[33] John Florio, Jack B. Henderson, Frederick L. Test, and Ramamurthy Hariharan. Characterization of forced convection heat transfer in decomposing, glass-filled polymer composites. *Journal of Composite Materials*, 25(11):1515–1539, 1991.